

Phantom and clinical evaluation of bone SPECT/CT image reconstruction with xSPECT algorithm

Noriaki Miyaji

Department of Nuclear Medicine, Cancer Institute Hospital of Japanese Foundation for Cancer Research

Kenta Miwa

Department of Radiological Sciences, School of Health Science, International University of Health and Welfare

Ayaka Tokiwa

Department of Radiological Sciences, School of Health Science, International University of Health and Welfare

Hajime Ichikawa

Department of Radiology, Toyohashi Municipal Hospital

Takashi Terauchi

Department of Nuclear Medicine, Cancer Institute Hospital of Japanese Foundation for Cancer Research

Mitsuru Koizumi

Department of Nuclear Medicine, Cancer Institute Hospital of Japanese Foundation for Cancer Research

Masahisa Onoguchi (✉ onoguchi@staff.kanazawa-u.ac.jp)

Department of Quantum Medical Technology, Graduate school of Medical Sciences, Kanazawa University

Original research

Keywords: xSPECT, bone SPECT, OSCGM, iteration number, novel reconstruction

Posted Date: June 15th, 2020

DOI: <https://doi.org/10.21203/rs.2.22777/v4>

License:  This work is licensed under a Creative Commons Attribution 4.0 International License.

[Read Full License](#)

Version of Record: A version of this preprint was published on June 29th, 2020. See the published version at <https://doi.org/10.1186/s13550-020-00659-5>.

Abstract

Background Two novel methods of image reconstruction, xSPECT Quant (xQ) and xSPECT Bone (xB) that use an ordered subset conjugate gradient minimizer (OSCGM) for SPECT/CT reconstruction have been proposed. The present study compares the performance characteristics of xQ, xB and conventional Flash3D (F3D) reconstruction using images derived from phantoms and patients.

Methods A custom-designed body phantom for bone SPECT was scanned using a Symbia Intevo (Siemens Healthineers) and reconstructed xSPECT images were evaluated. The phantom experiments proceeded twice with different activity concentrations and sphere sizes. A phantom with 28-mm spheres containing a ^{99m}Tc -background and tumor-to-normal bone ratios (TBR) of 1, 2, 4 and 10, were generated and convergence property against various TBR was evaluated across 96 iterations. A phantom with four spheres (13-, 17-, 22-, and 28-mm diameters), containing a ^{99m}Tc -background at TBR4, was also generated. The full width at half maximum of an imaged spinous process (10 mm), coefficients of variance (CV), contrast-to-noise ratio (CNR) and recovery coefficients (RC) were evaluated after reconstructing images of a spine using Flash 3D (F3D), xQ and xB. We retrospectively analyzed images from 20 patients with suspected bone metastases (male, $n = 13$) were acquired using [^{99m}Tc]Tc-(H)MDP SPECT/CT, then CV and standardized uptake values (SUV) at the 4th vertebral body (L4) were compared after xQ and xB reconstruction in a clinical setup.

Results Mean activity concentrations with various TBR converged according to increasing numbers of iterations. The spatial resolution of xB was considerably superior to xQ and F3D, and it approached almost the actual size regardless of the iteration numbers during reconstruction. The CV and RC were better for xQ and xB than for F3D. The CNR peaked at 24 iterations for xQ and 48 iterations for F3D and xB, respectively. The RC between xQ and xB significantly differed at lower numbers of iterations but were almost equivalent at higher numbers of iterations. The reconstructed xQ and xB images of the clinical patients showed a significant difference in the SUV_{max} and SUV_{peak}.

Conclusions The reconstructed xQ and xB images were more accurate than those reconstructed conventionally using F3D. The xB for bone SPECT imaging offered essentially unchanged spatial resolution even when the numbers of iterations did not converge. The xB reconstruction further enhanced SPECT image quality using CT data. Our findings provide important information for understanding the performance characteristics of the novel xQ and xB algorithms.

Background

Traditional bone imaging using ^{99m}Tc -labeled phosphate compounds is widely applied as diagnostic tools for detecting osseous metastases and staging malignant disease [1-3]. Hybrid bone imaging using single-photon emission computed tomography/computed tomography (SPECT/CT) can enhance image quality due to attenuation correction (AC), scatter correction (SC) and precisely localized tracer uptake. Römer et al. showed that 92% of indeterminate lesions could be correctly classified by SPECT/CT with a

pronounced benefit for bone lesions [4]. Utsunomiya et al. also reported significantly improved diagnostic confidence for fused SPECT/CT image datasets compared with side-by-side views of images using both SPECT and CT modalities [5]. Hybrid SPECT/CT imaging in three dimensions (3D) has overcome the problem of planar bone imaging, which has high sensitivity, but low specificity, and thus improved the accuracy of diagnosing bone lesions [6, 7].

Recent advances in SPECT technology have included not only hardware but also software, such as image reconstruction algorithms. Absolute quantitation of ^{99m}Tc bone SPECT/CT is becoming feasible as a diagnostic tool and as a means of monitoring treatment effects [8,9]. Previous phantom and clinical studies have found that the quantitative accuracy of SPECT imaging using ^{99m}Tc is within $\pm 10\%$ [10, 11]. A multicenter study of four SPECT/CT systems also found that quantitative accuracy was maintained within 10% using 3D iterative reconstruction with AC, SC, and resolution recovery [12]. However, more reliable quantitative data are needed before quantitative bone SPECT imaging could become a standard clinical diagnostic procedure. Currently, the need to develop novel SPECT imaging techniques associated with absolute SPECT quantitation has been discussed in terms of cost, standardized uptake values (SUV) and dosimetry [13-15]. Quantitative SPECT/CT can overcome the downsides of positron emission tomography and has thus contributed to the rapid spread of quantitative nuclear medicine applications [16,17].

Improved spatial resolution of SPECT images helps to improve the quantitation, detection, and precise localization of small lesions [18]. However, the spatial resolution of SPECT images remains poor. Tsui et al. suggested that multimodal image reconstruction would remarkably improve SPECT image quality [19]. Kuwert et al. also focused on quantitation and multimodal reconstruction as a methodological advance to further increase the value of bone SPECT/CT imaging [13]. The impact of using multimodal reconstruction methodology in SPECT imaging should be better quantifiability and excellent diagnostic confidence, although this awaits validation.

Siemens[®] has introduced a technology called “xSPECT”, which includes a novel iterative image reconstruction algorithm (ordered subset conjugate gradient minimizer; OSCGM) based on conventional ordered subset expectation maximization (OSEM; Flash 3D; F3D) to improve multimodal alignment in image space, and thus enhance image quality. Onoguchi et al. described the differences between OSEM and OSCGM algorithms in detail [20]. Briefly, the xSPECT technology applies the Mighell merit function to suppress noise caused by the fast convergence of OSCGM reconstruction. Additionally, National Institute of Standards and Technology (NIST) traceable calibration ^{57}Co point sources with 3% uncertainty (99% confidence level [CI]) were introduced by Siemens[®] to standardize quantitative ^{99m}Tc -SPECT. The SPECT voxel counts based on accurate correction can be converted to activity concentrations (Bq/mL) using a system planar sensitivity correction factor measured with a ^{57}Co source during reconstruction. This method of quantitative reconstruction is called “xSPECT Quant” (xQ). Siemens[®] also concurrently released bone-specific software with xSPECT features called “xSPECT Bone (xB)” [21], in which higher-resolution CT data were added to enhance reconstructed images at tissue boundaries. Therefore, xB

produces images of tracer distribution with far better resolution than F3D [22]. Some clinical reports have described that xB bone SPECT images are more precise in terms of localization and offer better diagnostic confidence in staging malignant disease [23-25].

The fundamental theory of xB is that the application of image space information, divided into six tissue classes by higher-resolution CT data, minimizes interpolation errors in information obtained from anatomical modalities. Those reconstructed images have high spatial recognition due to denser spatial sampling. In contrast, xQ applies a CT-derived reconstruction mask to reduce background noise [26]. A comparison of the two reconstruction methods revealed unexpected behavior of xQ, which caused a decrease in the image quality of >2 subsets [27, 28]. For both xQ and xB, developers also found that noise is lower, and resolution is higher in 3- than 6-degree sampling [29]. Quantitative and physical indexes such as recovery coefficients (RC), SUV and noise characteristics typically depend on image reconstruction and the reconstruction parameters. Although xSPECT imaging also depends on different reconstruction parameters, its impact has not yet been clarified. The present study aimed to determine the performance characteristics of the novel xSPECT algorithm. To our knowledge, this is the first attempt to clarify the functional differences between xQ and xB based on phantom measurements and clinical data.

Methods

Data acquisition and reconstruction

All imaging data were acquired using a Symbia Intevo16 hybrid SPECT/CT system (Siemens Healthineers, Erlangen, Germany) comprising an integrated dual-head SPECT camera with a 16-slice helical CT scanner. We acquired SPECT images under the following parameters: $\pm 7.5\%$ energy window at 140 keV with a lower scatter window of 15%, 1.27" crystal thickness, low-energy high-resolution collimator, 256 \times 256 matrix with 2.0-mm pixels and a total of 120 projections of 15 s/view over 360° in a non-circular orbit continuous acquisition mode. Immediately following SPECT acquisition, CT images were acquired at 130 KV and 70 ref mA using adaptive dose modulation (CARE Dose 4D; Siemens Healthineers) with a 512 \times 512 matrix, pitch 1.5, 0.8-s rotation and 2 \times 1.5-mm collimation. The CT data were reconstructed at a 3.0-mm slice thickness using a B31s attenuation filter (Siemens Healthineers).

We reconstructed the SPECT images using the algorithms F3D, xQ and xB and a 6-mm 3D Gaussian filter with various combinations of one fixed subset and 1-96 iterations. The OSEM based F3D is equipped with depth-dependent 3D resolution recovery using the Gaussian point-spread functions. The OSCGM based xQ and xB are equipped with depth-dependent 3D resolution recovery using actual measured point-spread functions map over entire FOV. The xB algorithm divides CT pixels into six tissue classes with smooth boundaries based on CT values or "zones" of air and lung, adipose, soft tissue, soft bone, cortical bone, metal material, and updates. The xB iterative operation can be weighted according to the corresponding zone class in the divided pixel; however, the iterative operation for each zone class based on the CT data does not increase the original count [21].

Cross-calibration of SPECT imaging

Counts from SPECT images reconstructed with F3D and xSPECT were converted to activity concentrations based on a cross-calibration factor (CCF) obtained from the relationship between the reconstructed counts and activity concentrations as well as system planar sensitivity, for quantitative comparisons.

In SPECT images using F3D, a circular region of interest (ROI) to measure SPECT count density (counts/mL) was placed at the center of the cylindrical phantom on the central slice and at ± 1 and ± 2 slices from the center. The CCF was automatically calculated using GI-BONE software (Aze, Tokyo, Japan) as the ratio of the actual activity concentration (measured by the dose calibrator) in the phantom at the time of scanning to the measured SPECT counts density per scan duration [30]. The dose calibrator used for cross-calibration was CRC-15R. (final calibration date by manufacturer: 4/19/2005) The dose calibrator was also confirmed and calibrated with a site-specific NIST-traceable $^{68}\text{Ge}/^{68}\text{Ga}$ source every 3 months [31, 32] (final calibration date in site: 12/18/2019). Therefore, we assume that the uncertainty of the measurement by the dose calibrator is small. The actual SUV was calculated as:

[Please see the supplementary files section to view the equation.]

Reconstruction with xQ and xB precisely determines images in units of Bq/mL that are converted using system planar sensitivity with an NIST traceable ^{57}Co source [21]. The system planar sensitivity is a necessary parameter to allow for conversion between the count rate and units of absolute activity. This is defined as a measure of how many counts the gamma camera detects for every unit of activity in its field of view. Therefore, system planar sensitivity was measured with the traceable point source without scattering and attenuation to realize accurate and reproducible quantitation [28, 33]. This source is recommended for all Siemens[®] users to improve SPECT quantitation. It was automatically converted to the quantitative SPECT/CT data by the VB10 software (Siemens Healthineers).

Phantom Studies

Phantom design

We custom-designed a physical three-dimensional phantom to determine the bone SPECT-specific distribution of activity and the linear attenuation coefficient (Figure 1). This phantom can be used to generate SPECT images of bone metastasis with a realistic abdomen contour [34]. The phantom contains a $^{99\text{m}}\text{Tc}$ solution to simulate soft tissue, the vertebral body, spinous and transverse process, and tumor region contained a bone-equivalent solution of K_2HPO_4 and $^{99\text{m}}\text{Tc}$ [35]. The phantom experiments were conducted twice using different activity concentrations and sphere sizes as follows. Tumor, normal bone, and soft tissues in the phantom were immersed in a solution of $^{99\text{m}}\text{Tc}$. In the first round of experiments, a body phantom with four 28-mm diameter spheres was set and acquired at tumor-to-

normal bone ratios (TBR) of 1, 2, 4 and 10 at a normal bone activity level of 50 kBq/mL. This phantom contained 8 kBq/mL of a ^{99m}Tc solution as the background activity of the soft tissue. That is, the boundary and the background do not differ at TBR1, but the difference in the activity concentration increases as a function a higher TBR. We determined the activity concentrations of the simulated soft tissue, normal bone, and tumor at 8, 50 and 200 kBq/mL, (TBR4), respectively, in second round of experiments using a phantom with 13-, 17-, 22-, 28-mm diameter spheres.

Figure 1

Data Analysis

The SPECT acquisition data in the first round of experiments were reconstructed using 1 subset and 1-96 iterations. We examined the effects of the reconstruction algorithms on various TBR in the 28-mm sphere and then determined the optimal reconstruction parameters based on the result of convergence characteristics. Phantom images containing simulated tumors of different sizes were continuously analyzed in terms of the spatial resolution of a 10-mm spinous process, the coefficient of variance (CV), the contrast-to-noise ratio (CNR) of the vertebral body and RC as quantitative parameters. We drew profile curves on the spinous process, measured the full width at half maximum (FWHM). The CV evaluated at an 80% circular ROI (ROI80%) placed at the center of the vertebral body. In addition, a total of sixty ROI80% including ± 1 and ± 2 slices were placed around the vertebral body to calculate as background CV. The CV was calculated as standard deviation (SD) divided by mean in the ROI. The CNR and RC at each sphere were determined by setting circular ROIs with diameters of 13-, 17-, 22-, 28-mm. The CNR at TBR 4 was calculated as $(H_s - H_{nb}) / \sigma_{nb}$, where, H_s and H_{nb} are the activity concentrations measured in the spheres and normal bone, respectively, and σ_{nb} is the voxel SD in the normal bone. The RC was defined as the ratio of the SPECT-based and the true activity concentration (kBq/mL) for each sphere.

Clinical study

Imaging protocol

We analyzed data from 20 consecutive patients who had undergone bone SPECT/CT imaging for metastatic prostate or breast cancer (male, $n = 13$; female, $n = 7$; median age, 62 years; range, 40–83 years; average weight, 65.2 ± 13.4 kg; range, 51.8–78.6 kg). The optimal parameters of the convergence characteristic in the phantom study was applied to the clinical reconstruction condition in xQ and xB. Bone SPECT/CT imaging proceeded from the abdomen to the pelvis ~2.5–4 h after delivering an intravenous injection of 1003.4 ± 102.8 MBq ^{99m}Tc -methylene diphosphonate ($[^{99m}\text{Tc}]\text{Tc-MDP}$; FUJIFILM Toyama Chemical, Tokyo, Japan) or hydroxymethylene diphosphonate ($[^{99m}\text{Tc}]\text{Tc-HMDP}$; Nihon Medi-

Physics, Tokyo, Japan). The average amount of injected ^{99m}Tc was 15.9 ± 2.8 (range, 13.1–18.7) MBq/kg. The Ethics Committee at the Cancer Institute Hospital of JFCR approved this clinical study (Approval no. 2015-1151). These clinical data were retrospectively analyzed, and the results did not influence any further therapeutic decision-making.

Data analysis

The noise characteristics and quantitative performance of the clinical SPECT image were analyzed at the level of the 4th vertebral body (L4) [36]. We adjusted and placed a ROI of 80% size on the center of the axial slice in the section after measured the ROI of the vertebral body guided by the CT boundaries of the fused SPECT/CT images. We normalized the SUV_{max} , SUV_{mean} and SUV_{peak} by the weight of each patient. An average and maximum concentration in milliliter within a ROI would produce an estimate of the SUV, which is defined here as SUV_{mean} and SUV_{max} , respectively. SUV_{peak} has been suggested as an alternative to SUV_{max} . SUV_{peak} within a setting ROI is an average SUV calculated within a fixed-size (this is a sphere with a diameter of approximately 1.2 cm to require a 1-cm³-volume spheric ROI), placed highest uptake region including maximum pixel value. Because this ROI encompasses several pixels, SUV_{peak} is assumed to be less affected by image noise than SUV_{max} . These data were analyzed using PETSTAT software (AdIn Research, Tokyo, Japan).

Figure 2

Statistical analysis

All SUV and CV indices in the xQ and xB groups were compared using Wilcoxon signed-ranks tests after evaluating the non-normal distribution using Kolmogorov-Smirnov tests. Values were considered statistically significant when $P < 0.05$. These data were statistically analyzed using SPSS Statistics software (IBM corp, Armonk, NY, USA).

Results

Phantom studies

Convergence for various TBR

Figure 3 shows the SPECT data reconstructed using between 1 and 96 iterations. Regardless of the reconstruction model and iteration number, the means were better than the maximum activity

concentrations for the two lowest TBR values (Fig. 3A and B) whereas those of the maximum activity concentrations were better results for the highest TBR values (Fig. 3C and D). In Figure 3D, the maximum activity concentrations were the highest with F3D, and better than those for both xQ and xB. On the other hand, the maximum activity concentration with xSPECT did not converge and increased in proportion to the iteration numbers. The mean activity concentration converged with increasing iterations regardless of the TBR. The mean activity concentrations of xQ and xB were essentially equivalent at >24 iterations. The mean activity concentration was lower for F3D than xQ and xB.

Figure 3

Spatial resolution

Figure 4 shows the spatial resolution of the spinous process for various iterations. The FWHM with xQ and F3D considerably improved when the iteration number increased, but the spatial resolution produced by the xB algorithm was optimal. The FWHM of the xQ and F3D reconstructions converged at about 15 and 20 mm, respectively. In contrast, the xB values remained similar to the actual size (10 mm) regardless of iteration numbers. Figure 5 shows the results of the xSPECT and F3D images with 1 subset and F3D images with 3 subsets at 48 iterations, respectively. The boundary of the vertebral body was visually indistinct on reconstructed F3D and xQ bone SPECT images, whereas it was clearly visible in the reconstructed xB images. In terms of background region, xB and F3D images with 1 subset produced clearer images than xQ. Also, the xQ with 1 subset and F3D with 3 subsets respectively was visually equivalent level.

Figure 4

Figure 5

Noise characteristics

Figure 6 shows the CV of the vertebral body and background region according to the number of iterations, respectively. The CV in vertebral body was higher F3D than xQ and xB as the iteration numbers increased, and the amount of noise was similar between xQ and xB. Those of xQ and xB at >24 iterations were both relatively stable at 0.2. On the other hand, the background CV of xQ significantly was inferior to other reconstruction. The CV of xB and F3D showed an equivalent value at 48 iteration numbers. Figure 7 shows the CNR in the vertebral body region according to the iteration numbers. The mean and max CNR were similar for each reconstruction. Although the mean CNR was better in the order of xB, xQ and F3D as the iteration numbers increased, the CNR of F3D and xB at > 48, and xQ at > 24 iterations decreased.

Figure 6

Figure 7

Recovery coefficient

Figure 8 shows the RC of the vertebral body for 12–96 iterations. The RC in all algorithms improved with increasing sphere size. The RC was relatively higher with xB, than with the other algorithms at 12 iterations, and the differences in the RC between xQ and xB were essentially equivalent as a function of the increasing numbers of iterations. The RC was lower for F3D than xQ and xB at the same number of iterations, but the RC of F3D after 36 iterations was better than that of xQ after 12 (Fig. 8G).

Figure 8

Clinical study

Table 1 shows the SUV_{max} , SUV_{peak} , SUV_{mean} and CV under clinical conditions. The quantitative SPECT values were much higher for some patients. The statistical findings showed a significant difference in the SUV_{max} and SUV_{peak} between xQ and xB. However, SUV_{mean} and CV on SPECT images reconstructed with xQ and xB did not significantly differ ($P > 0.05$).

Table 1. Values for SUV_{mean} , SUV_{max} , SUV_{peak} and CV of the 4th vertebral body in xQ and xB reconstructions

Quantitative indices	Reconstruction type	Mean \pm SD	Min - Max	P value
SUV_{mean}	xQ	7.10 \pm 5.81	2.50 - 30.34	0.084
	xB	7.03 \pm 5.91	2.29 - 30.76	
SUV_{max}	xQ	12.29 \pm 11.84	4.87 - 58.16	0.021
	xB	11.90 \pm 12.16	4.67 - 59.07	
SUV_{peak}	xQ	11.63 \pm 11.25	4.68 - 55.73	0.001
	xB	11.24 \pm 11.37	4.56 - 55.52	
CV	xQ	0.28 \pm 0.17	0.13 - 0.80	0.141
	xB	0.26 \pm 0.17	0.12 - 0.69	

Discussion

We validated novel xSPECT and conventional F3D reconstruction algorithms using experimental data derived from phantoms. Differences between xB and xQ were quantified based on clinical data from patients. The phantom study found image quality and quantitative accuracy of xSPECT was considerably superior to those of F3D. However, background noise obviously differed visually for xQ without weighted correction compared with F3D due to increasing noise caused by fast convergence. We also found that the high spatial resolution of xB was maintained regardless of the iteration numbers. The SUV_{max} and the SUV_{peak} in the clinical study significantly differed between xQ and xB; thus, we concluded that xB could serve as an essential diagnostic tool for bone SPECT imaging in terms of quantitative accuracy and spatial resolution.

Regardless of the reconstruction models, the maximum activity concentration in the TBR1 and TBR2 spheres was overestimated compared with actual activity concentration (Fig. 3). This can be explained by

the fact that the maximum activity concentration in the sphere theoretically increased because of increasing statistical noise at lower counts [37]. The activity is pushed into the contours of the sphere due to the spatial constraint by a CT-based intensity masking for OSCGM. Tran-Gia et al. showed the mean xQ inside the sphere remained relatively similar to F3D, the distribution in the profile curve was drastically changed compared to F3D. The maximum in the sphere center was increasing, while the edge was decreasing [29]. Therefore, no convergence was reached for the SUV_{max} of xSPECT in Figure 3 and the recovery of xSPECT was highly dependent on the iteration number. In contrast, F3D for higher TBRs is independent of the total iteration numbers, the maximum activity concentration of the F3D exceeded those of xSPECT (Fig. 3D). The merit function incorporated in xSPECT might enhance noise suppression as a function of higher activity concentration. However, this effect reduced for higher iteration numbers because xSPECT does not converge. The xSPECT reconstruction has several unknown features, so this is only one potential explanation. On the other side, the mean activity concentration approached the actual activity concentration at lower TBR. When the activity concentrations of tumor and normal bone were equal (TBR = 1), spill-out by partial volume did not occur because the activity concentrations inside and outside the ROI were almost equivalent. TBR 1 was slightly overestimated due to the activity concentration being increased by the statistical noise. At a higher TBR, the mean activity concentration was underestimated due to spillage from the sphere into the background [38]. The quantitative differences between F3D and xSPECT are influenced by statistical noise based on convergence and by partial volume effects caused by lower spatial resolution. Our results showed that the mean activity concentrations for F3D essentially converged within 48 iterations, but those for xQ and xB similarly converged at >24 iterations. The FWHM for the xQ after 36 iterations converged and the RC between the xB and xQ was almost equivalent at over 36 iterations. The maximum activity concentrations with xSPECT did not converge even for high iteration numbers as shown in Figure 3. The iteration numbers is associated with a trade-off between signal and noise. Considering the increase in noise, we determined that 30 iterations were the most appropriate for xSPECT reconstruction in clinical practice.

The FWHM of F3D after >36 iterations was better than xQ after 12 iterations that have not fully convergence; however, the FWHM with xQ and F3D considerably improved and fully converged at ~15 and 20 mm, respectively, at a high number of iterations. Therefore, image quality was better for xQ than F3D at the appropriate parameter. In contrast, the xB algorithm divided into zone class generated unique results, unlike the observed xQ. The spatial resolution for xB remained almost unchanged even for lower iteration numbers, and the actual size of 10 mm was almost achieved. The zone class of each tissue was based on high-resolution CT images with delineated edges; therefore, the FWHM of xB reflects the relationship to CT resolution. Additionally, the xB iterative operation is weighted by zero or other value according to the corresponding zone class in the divided pixel [21]. We considered that not only bone classes weighted by the optimal value, but also non-bone classes weighted by zero with a zonal map were responsible for the improved spatial resolution using the xB technology.

The xSPECT can compensate for SPECT images by applying the merit function in the higher noise caused by the faster convergence of OSCGM reconstruction. This method of reconstruction adopts the

Mighell-modified chi-squared gamma statistic algorithm. Shinohara et al. indicated that Mighell-modified noise suppression was better than other image reconstructions based on chi-square statistics [39]. The CV of xQ and xB did not exceed that of F3D at 12 iterations regardless of the iteration numbers. Thus, xSPECT with the Mighell-modified merit function considerably suppressed noise compared with F3D algorithms at the same number of iterations. For one subset of reconstructed images, a more apparent problem is the increasing image noise in the background region and in hot spheres according to the iteration numbers. The background noise in the xQ image rapidly increased and significantly was inferior to the other reconstructed images at 48 iterations (Fig. 5 and Fig. 6). However, Armstrong et al. reported that the greatest CNR for xQ is achieved at 48 iterations for one subset [28]. Our findings indicated that the greatest CNR for xQ was at 24 iterations and that the RC was higher than for F3D at 48 iterations (Figs. 7 and Fig. 8H). On the other hand, xB suppressed image noise more effectively than F3D and xQ (Fig. 6). Because xB reconstruction has weighted correction for every zone class, the impact of noise suppression differed between xQ and xB [40]. The CNR in xB reached the maximum at 48 iterations, and noise suppression decreased in xB at > 48 iterations. In regions with inadequate uptake such as soft tissues, the xQ based on the OSCGM algorithm might lead not only to an increased CV according to iteration setting, but also to ramifications for lesion detectability. Therefore, the xQ requires further careful optimization of the iteration numbers than F3D and xB.

The present study assessed data from 20 patients with suspected bone metastases. The SPECT values of measured L4 had a wide SUV range because some patients had various pathologies (bone metastasis (n = 7), degenerative (n = 5) and trauma (n = 3)). Our clinical study found a significant difference in SUV_{peak} , SUV_{max} , and this quantitative difference between xQ and xB could be interpreted as noise suppression owing to weighted correction based on zone map system. Because the SUV_{peak} is less susceptible to statistical noise compared with SUV_{max} [36], it significantly differed between xQ and xB ($p = 0.001$). The clinical xB image with high resolution can not only reveal bone microlesions but also improve diagnostic confidence [23]. Therefore, we considered that clinical evaluation for xB images with SUV_{peak} could provide more accurate and reliable diagnostics. To calculate SUV_{peak} entails expressing the maximum average voxel value within a spherical volume of 1 cm^3 , but the xB is useful to enhance diagnostics for bone SPECT images in terms of quantitative and qualitative superiority. However, the quantitative variation caused by misalignments such as motion and respiratory errors during clinical scanning is a concern. Reconstruction using the xB algorithm might behave differently due to the unique zone map system. Therefore, misalignment between SPECT and CT images due to respiratory errors such as those caused by the ribs and sternum should be considered when clinically applying xB.

The present study has several limitations. The reconstructed SPECT images were assessed using different cross-calibration methods. The CCF on quantitative SPECT images varied depending on the activity concentration [41]. Thus, slight quantitative errors might arise between the F3D and xSPECT models. In addition, the body type of the 20 patients and the amounts of injected tracer were essentially standard (average, $15.9 \pm 2.8\text{ MBq/kg}$). We could not consider dependence on physique into consideration, and the effects of factors such as counts, and scattering remain unclear. Further study is

required to assess the relationship between body type and the quality of images reconstructed using the xSPECT algorithm.

Conclusions

Bone images were qualitatively and quantitatively improved when reconstructed using OSCGM-based xSPECT (xQ and xB) compared with the OSEM-based F3D reconstruction. The quality of images under optimized xB reconstruction conditions was better because of sharper demarcation and lower background noise. One unique aspect of the bone structures in xB reconstructions is that the image content such as spatial resolution was independent of the iteration numbers. Our findings provide important information that should facilitate understanding of the performance characteristics of the novel xQ and xB algorithms.

Abbreviations

xQ	xSPECT Quant
xB	xSPECT Bone
OSCGM	Ordered subset conjugate gradient minimizer
F3D	Flash 3D
FWHM	Full width at half maximum
CV	Coefficients of variance
RC	Recovery coefficients
SUV	Standardized uptake value
L4	4 th vertebral body
AC	Attenuation correction
SC	Scatter correction
SPECT/CT	Single-photon emission computed tomography/computed tomography
OSEM	Ordered subset expectation maximization
CCF	Cross-calibration factor
TBR	Tumor-to-normal bone ratios

ROI Regions of interest

Declarations

Ethics approval and consent to participate

The Ethics Committee at the Cancer Institute Hospital of JFCR approved this clinical study (approval no. 2015-1151). The results of this retrospective study did not influence any further therapeutic decision-making.

Consent for publication

Not applicable

Availability of data and material

All data generated or analyzed during this study are included in this published article

Competing interests

The authors declare that they have no competing interests

Funding

None

Authors' contributions

NM contributed to the study design, phantom data acquisition and analysis of the data. KM and MO contributed to the study design, analysis of the data, and draft and critical revision of the manuscript. HI and AT contributed to the preparation of the study and critical revision of the manuscript. HI contributed to phantom data acquisition and interpretation. TT and MK contributed to the critical revision of the manuscript. All authors read and approved of the final manuscript.

Acknowledgements

We would like to thank the staff at the Diagnostic Imaging Center in Cancer Institute Hospital of JFCR. Parts of this manuscript were presented at the 2018 SNMMI Annual Meeting and the corresponding abstract published in JNM (J Nucl Med May 1, 2018 vol. 59 no. supplement 1 1792).

Contributor Information

Noriaki Miyaji Email: noriaki.miyaji@gmail.com.

Kenta Miwa, Email: kenta5710@gmail.com.

Ayaka Tokiwa, Email: 1415079@g.iuhw.ac.jp.

Hajime Ichikawa, Email: ballocks10@yahoo.co.jp.

Takashi Terauchi, Email: takashi.terauchi@jfcr.or.jp.

Mitsuru Koizumi, Email: mitsuru@jfcr.or.jp.

Masahisa Onoguchi, Phone: +81-76-265-2526, Email: onoguchi@staff.kanazawa-u.ac.jp.

References

1. Krasnow AZ, Hellman RS, Timins ME, Collier BD, Anderson T, Isitman AT. Diagnostic bone scanning in oncology. *Semin Nucl Med.* 1997;27(2):107-141.
2. Hamaoka T, Madewell JE, Podoloff DA, Hortobagyi GN, Ueno NT. Bone imaging in metastatic breast cancer. *J Clin Oncol.* 2004;22:2942–2953.
3. Shen G, Deng H, Hu S, et al. Comparison of choline-PET/CT, MRI, SPECT, and bone scintigraphy in the diagnosis of bone metastases in patients with prostate cancer: a meta-analysis. *Skeletal Radiol.* 2014;43(11):1503-1513.
4. Römer W, Nömayr A, Uder M, Bautz W, Kuwert T. SPECT-guided CT for evaluating foci of increased bone metabolism classified as indeterminate on SPECT in cancer patients. *J Nucl Med.* 2006;47(7):1102-1106.
5. Utsunomiya D, Shiraishi S, Imuta M, Tomiguchi S, Kawanaka K, Morishita S, et al. Added value of SPECT/CT fusion in assessing suspected bone metastasis: comparison with scintigraphy alone and nonfused scintigraphy and CT. *Radiology.* 2006;238:264-271.
6. Even-Sapir E. Imaging of Malignant Bone Involvement by Morphologic, Scintigraphic, and Hybrid Modalities. *J Nucl Med.* 2005;46(8):1356-1367.
7. Damle NA, Bal C, Bandopadhyaya GP, Kumar L, Kumar L, Kumar P, Malhotra A, et al. The role of 18F-fluoride PET-CT in the detection of bone metastases in patients with breast, lung and prostate carcinoma: a comparison with FDG PET/CT and 99mTc-MDP bone scan. *Jpn J Radiol.* 2013;31(4):262-269.
8. Cachovan M, Vija AH, Hornegger J, Kuwert T. Quantification of ^{99m}Tc-DPD concentration in the lumbar spine with SPECT/CT. *EJNMMI Res.* 2013;3(1):45.
9. Beck M, Sanders JC, Ritt P, Reinfelder J, Kuwert T. Longitudinal analysis of bone metabolism using SPECT/CT and ^{99m}Tc-diphosphonopropanedicarboxylic acid: comparison of visual and quantitative analysis. *EJNMMI Res.* 2016;6(1):60.
10. Ritt P, Vija AH, Hornegger J, Kuwert T. Absolute quantification in SPECT. *Eur J Nucl Med Mol Imaging.* 2011;38 Suppl 1:S69-77.

11. Bailey DL, Willowson KP. An evidence-based review of quantitative SPECT imaging and potential clinical applications. *J Nucl Med.* 2013;54(1):83-89.
12. Seret A, Nguyen D, Bernard C. Quantitative capabilities of four state-of-the-art SPECT-CT cameras. *EJNMMI Res.* 2012;2(1):45.
13. Kuwert, T. Skeletal SPECT/CT: a review. *Clin Transl Imaging.* 2014;2:505–517.
14. Ross, J.C., Vilić, D., Sanderson, T, Vöö S, Dickson J. Does quantification have a role to play in the future of bone SPECT? *Eur J Hybrid Imaging.* 2019;3:8.
15. Dickson, J., Ross, J. & Vöö, S. Quantitative SPECT: the time is now. *EJNMMI Phys* 2019;6:4.
16. Israel O, Pellet O, Biassoni L, De Palma D, Estrada-Lobato E, Gnanasegaran G, et al. Two decades of SPECT/CT – the coming of age of a technology: An updated review of literature evidence. *Eur J Nucl Med Mol Imaging.* 2019; 46(10): 1990–2012.
17. Mariani G, Strauss HW. Positron emission and single-photon emission imaging: synergy rather than competition. *Eur J Nucl Med Mol Imaging.* 2011; 38(7):1189-1190.
18. van der Vos CS, Koopman D, Rijnsdorp S, Arends AJ, Boellaard R, van Dalen JA, et al. Quantification, improvement, and harmonization of small lesion detection with state-of-the-art PET. *Eur J Nucl Med Mol Imaging.* 2017;44(Suppl 1):4-16.
19. Tsui BMW, Zhao X, Frey EC, Gullberg GT. Comparison between ML-EM and WLS-CG algorithms for SPECT image reconstruction. *IEEE Trans Nucl Sci.* 1991;38:1766-1772.
20. Onoguchi M, Konishi T, Shibutani T, Matsuo S, Nakajima K. Technical aspects: Image reconstruction. *Ann Nucl Cardiol.* 2016;2:68-72.
21. Vija AH. Introduction to xSPECT technology: evolving multi-modal SPECT to become context-based and quantitative. In: Vija AH (ed) *Molecular Imaging White Paper: Siemens Medical Solutions USA, Inc., Molecular Imaging* 2014.
22. Ma J, Vija AH. Evaluation of quantitation accuracy for xSPECT. Paper presented at: Nuclear Science Symposium and Medical Imaging Conference (NSS/MIC), 2015 IEEE, 2015. doi: 10.1109/NSSMIC.2015.7582030.
23. Duncan I, Ingold N. The clinical value of xSPECT/CT Bone versus SPECT/CT. A prospective comparison of 200 scans. *Eur J Hybrid Imaging.* 2018;2(1):4.
24. Delcroix O, Robin P, Guillou M, Le Duc-Pennec A, Alavi Z, Le Roux PY, et al. A new SPECT/CT reconstruction algorithm: reliability and accuracy in clinical routine for non-oncologic bone diseases. *EJNMMI Res.* 2018;8(1):14.
25. Kuji I, Yamane T, Seto A, Yasumizu Y, Shirotake S, Oyama M. Skeletal standardized uptake values obtained by quantitative SPECT/CT as an osteoblastic biomarker for the discrimination of active bone metastasis in prostate cancer. *Eur J Hybrid Imaging.* 2017;1(1):2.
26. Willowson K, Bailey DL, Baldock C. Quantitative SPECT reconstruction using CT-derived corrections. *Phys Med Biol.* 2008;53(12):3099–112.

27. Tran-Gia, Lassmann M. Characterization of Noise and Resolution for Quantitative ^{177}Lu SPECT/CT with xSPECT Quant. *J Nucl Med* 2019; 60:50–59
28. Armstrong IS, Hoffmann SA. Activity concentration measurements using a conjugate gradient (Siemens xSPECT) reconstruction algorithm in SPECT/CT. *Nucl Med Commun.* 2016;37(11):1212-1217.
29. Vija AH. Characteristics of the xSPECT Reconstruction Method. Siemens molecular imaging white paper. 2017.
30. Nakahara T, Daisaki H, Yamamoto Y, Imori T, Miyagawa K, Okamoto T, et al. Use of a digital phantom developed by QIBA for harmonizing SUVs obtained from the state-of-the-art SPECT/CT systems: a multicenter study. *EJNMMI Res.* 2017;7(1):53.
31. Zimmerman BE, Cessna JT. Development of a traceable calibration methodology for solid $^{68}\text{Ge}/^{68}\text{Ga}$ sources used as a calibration surrogate for ^{18}F in radionuclide activity calibrators. *J Nucl Med.* 2010;51(3):448-453.
32. Miyaji N, Miwa K, Wagatsuma K, Umeda T, Murata T, Takiguchi T, et al. Quality control of dose calibrator using a traceable syringe-type $^{68}\text{Ge}/^{68}\text{Ga}$ calibration source. *Nihon Hoshasen Gijutsu Gakkai Zasshi.* 2013;69(12):1379-1386.
33. Miyaji N, Miwa K, Motegi K, Umeda T, Wagatsuma K, Fukai S, et al. Validation of Cross-calibration Schemes for Quantitative Bone SPECT/CT Using Different Sources under Various Geometric Conditions. *Nihon Hoshasen Gijutsu Gakkai Zasshi.* 2017;73(6):443-450.
34. Ichikawa H, Miwa K, Matsutomo N, Watanabe Y, Kato T, Shimada H. Development of a Novel Body Phantom with Bone Equivalent Density for Evaluation of Bone SPECT. *Nihon Hoshasen Gijutsu Gakkai Zasshi.* 2015;71(12):1235-1240.
35. Iida H, Hori Y, Ishida K, Imabayashi E, Matsuda H, Takahashi M, et al. Three-dimensional brain phantom containing bone and grey matter structures with a realistic head contour. *Ann Nucl Med.* 2013;27(1):25-36.
36. Kaneta T, Ogawa M, Daisaki H, Nawata S, Yoshida K, Inoue T. SUV measurement of normal vertebrae using SPECT/CT with Tc-99m methylene diphosphonate. *Am J Nucl Med Mol Imaging.* 2016;6(5):262-268.
37. Akamatsu G, Ikari Y, Nishida H, Nishio T, Ohnishi A, Maebatake A, et al. Influence of Statistical Fluctuation on Reproducibility and Accuracy of SUVmax and SUVpeak: A Phantom Study. *J Nucl Med Technol.* 2015;43(3):222-226.
38. Soret M, Bacharach SL, Buvat I. Partial-volume effect in PET tumor imaging. *J Nucl Med.* 2007;48(6):932-945.
39. Shinohara H, Hashimoto T. An Error Evaluation of Iterative Image Reconstruction Methods Using Chi-Square (χ^2) Statistic Minimization for Poisson-Distributed Projection Data. *Igaku Butsuri.* 2018;38(3):113-128.

40. Okuda K, Fujii S, Sakimoto S. Impact of Novel Incorporation of CT-based Segment Mapping into a Conjugated Gradient Algorithm on Bone SPECT Imaging: Fundamental Characteristics of a Context-specific Reconstruction Method. *Asia Ocean J Nucl Med Biol.* 2019;7(1):49-57.
41. Matsutomo N, Matsumoto S, Yamamoto T, Sato E. Validation of a calibration method using the cross-calibration factor and system planar sensitivity in quantitative single-photon emission computed tomography imaging. *Radiol Phys Technol.* 2017;10(4):439-445.

Figures

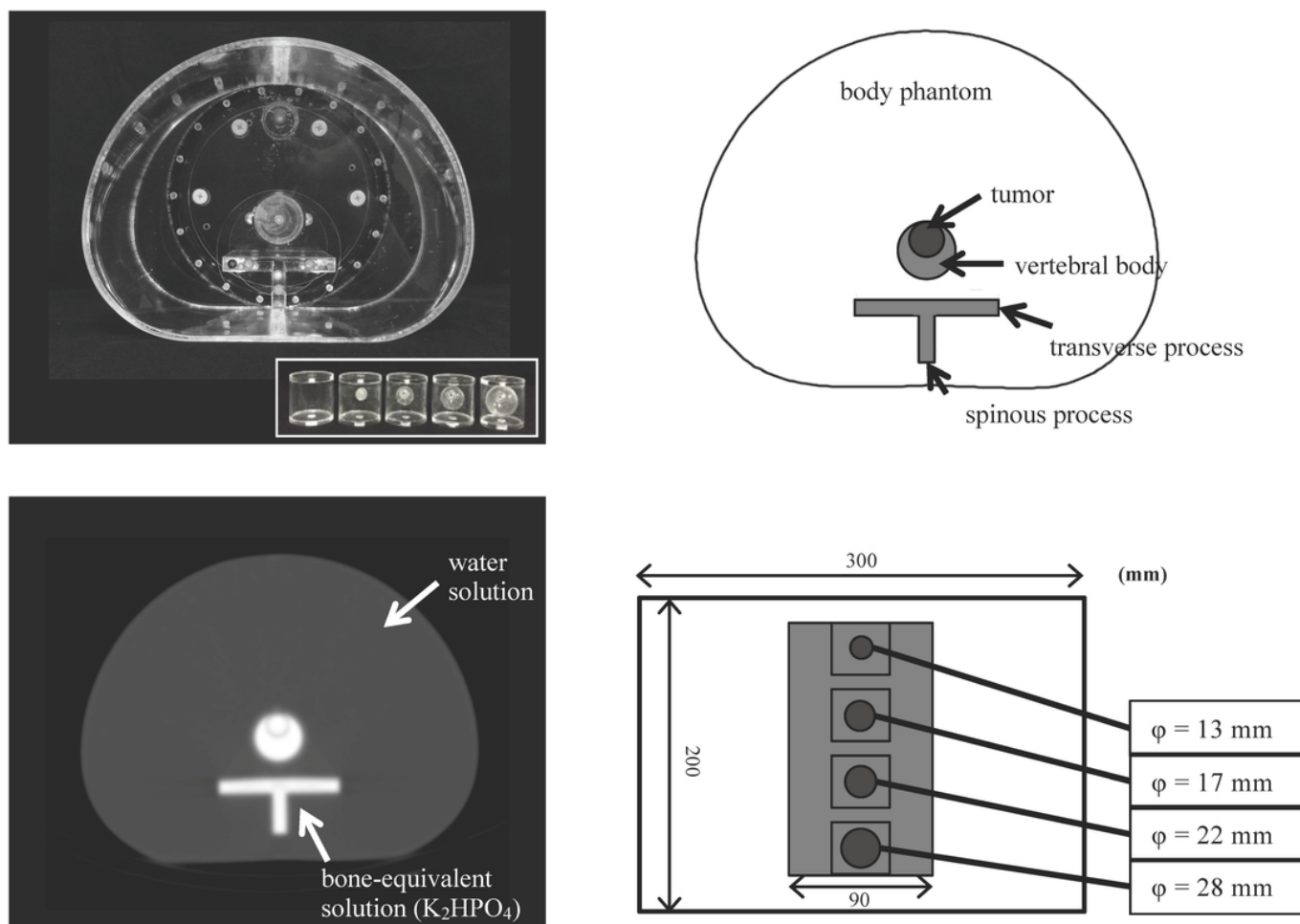


Figure 1

Custom-designed phantom configured with vertebral body, spinous and transverse process, and a sphere set inside vertebral body to simulate bone metastasis.

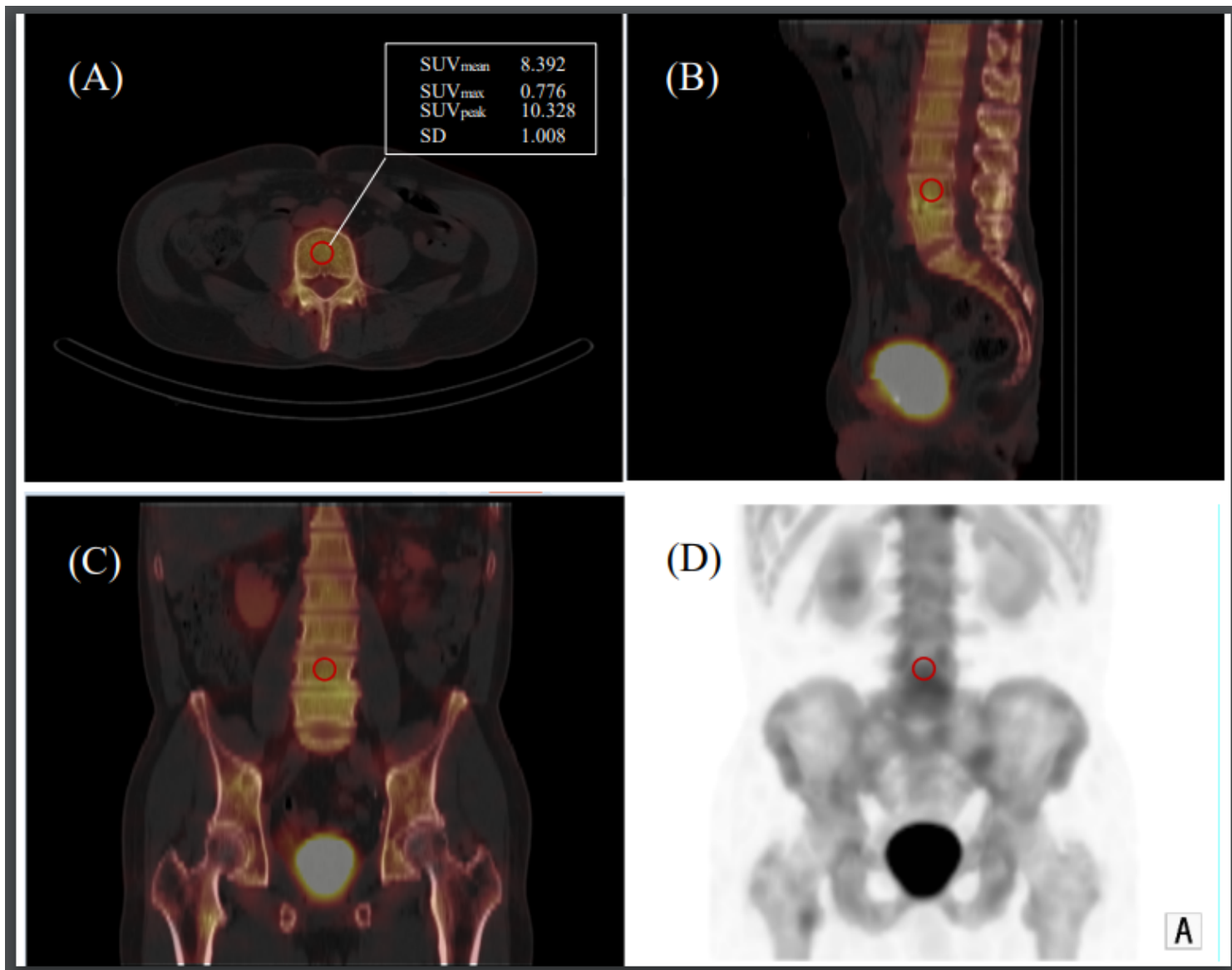


Figure 2

We set ROI80% (red circle) at the center of xB imaged based on a fused axial image, then adjusted by sagittal and coronal images. (A), Fused axial image; (B), Fused sagittal image; (C), Fused coronal image; (D), MIP image.

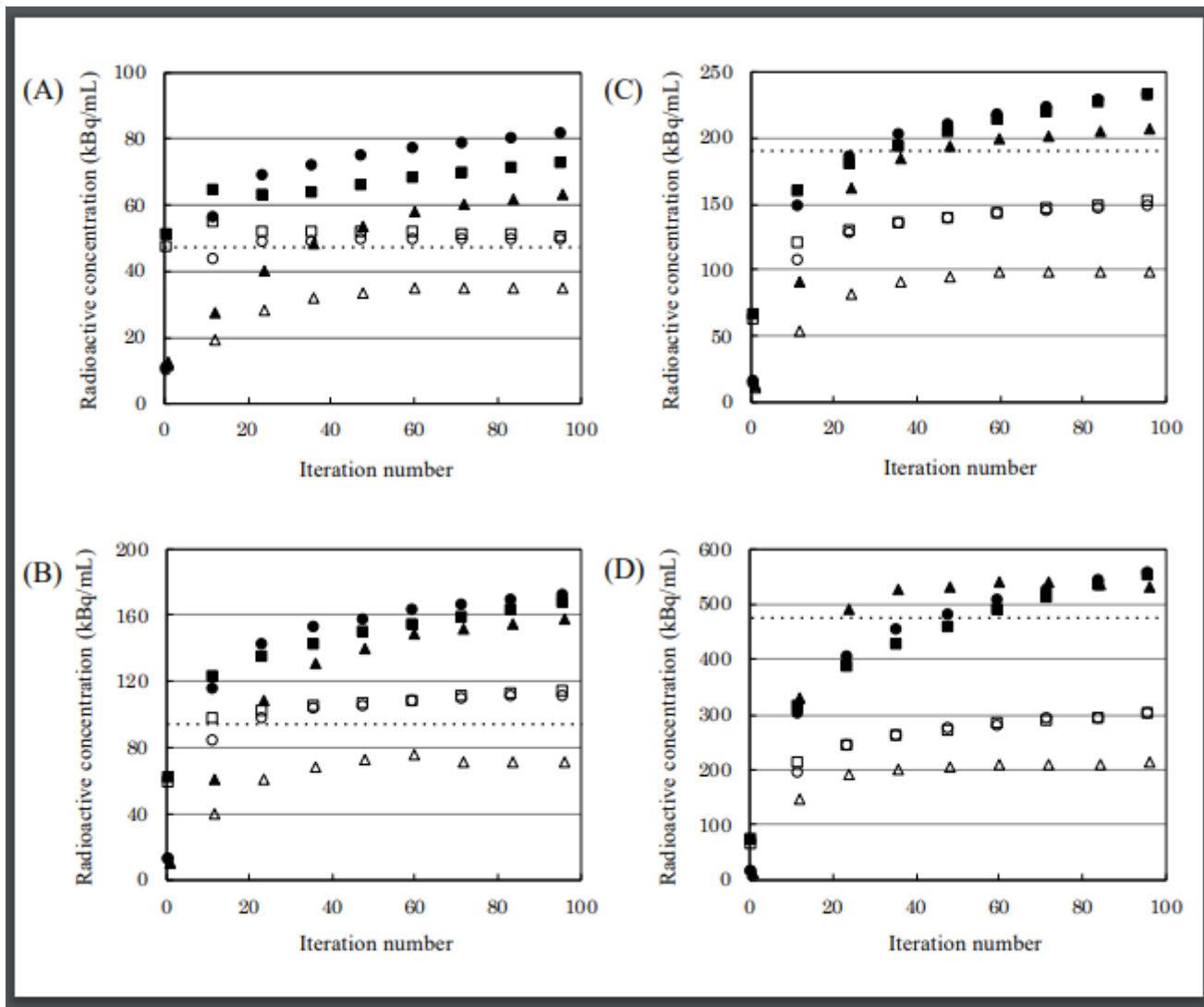


Figure 3

Reconstruction plots showing quantitative distribution in TBR1 (A), 2 (B), 4 (C) and 10 (D). The filled and unfilled symbols indicate maximum and mean activity concentrations, respectively. The dotted line is the actual activity concentration of phantom. \blacksquare , Flash 3D (F3D); \square , xSPECT Quant (xQ); \triangle , xSPECT Bone (xB).

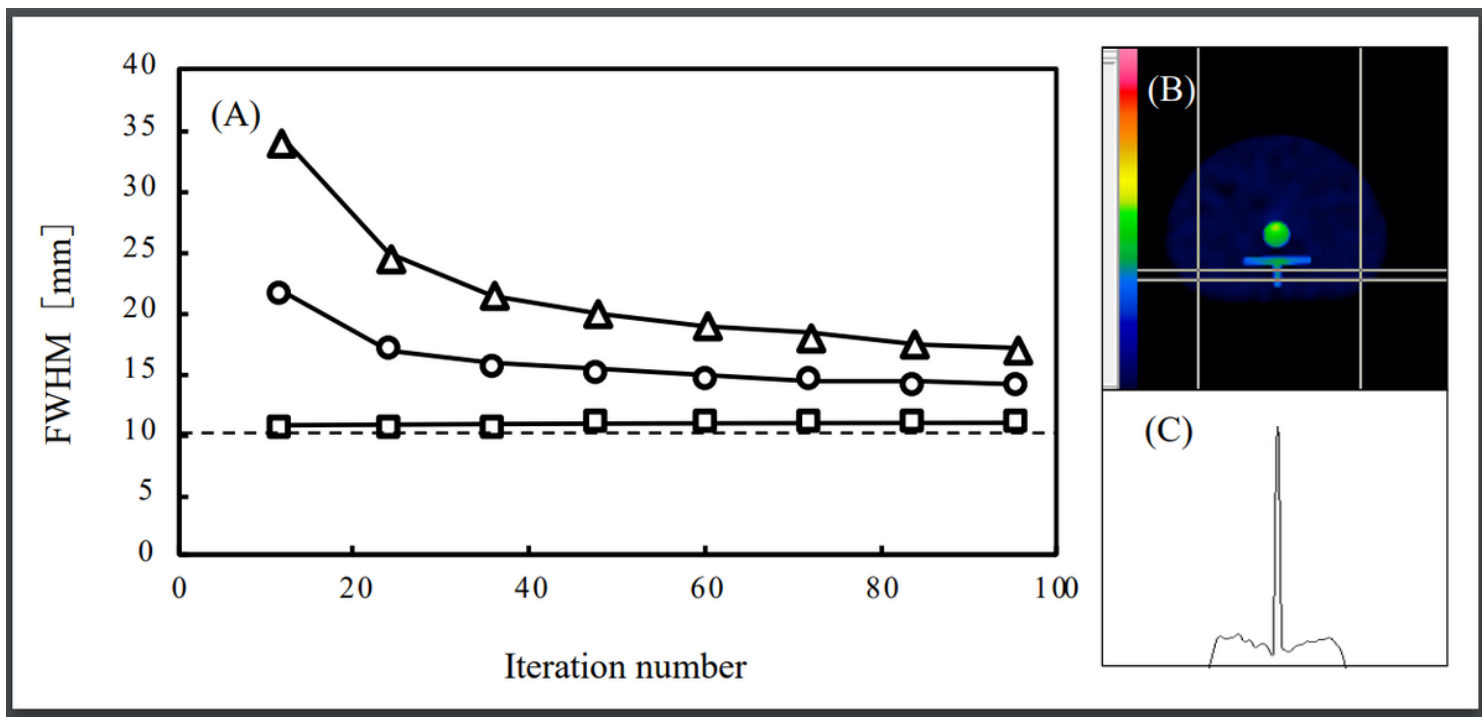


Figure 4

The FWHM measurement shown by the profile curve on the spinous process cross-section. (A), Spatial resolution of three reconstructions at various iterations. The dotted line is the actual size of the phantom. □, Flash 3D (F3D); ○, xSPECT Quant (xQ); △, xSPECT Bone (xB). (B), A sample measurement of an xB image at 12 iteration numbers. (C), A measurement profile of an xB image at 12 iteration numbers. The plateau signal around the spinous process is a distribution of background region in the phantom.

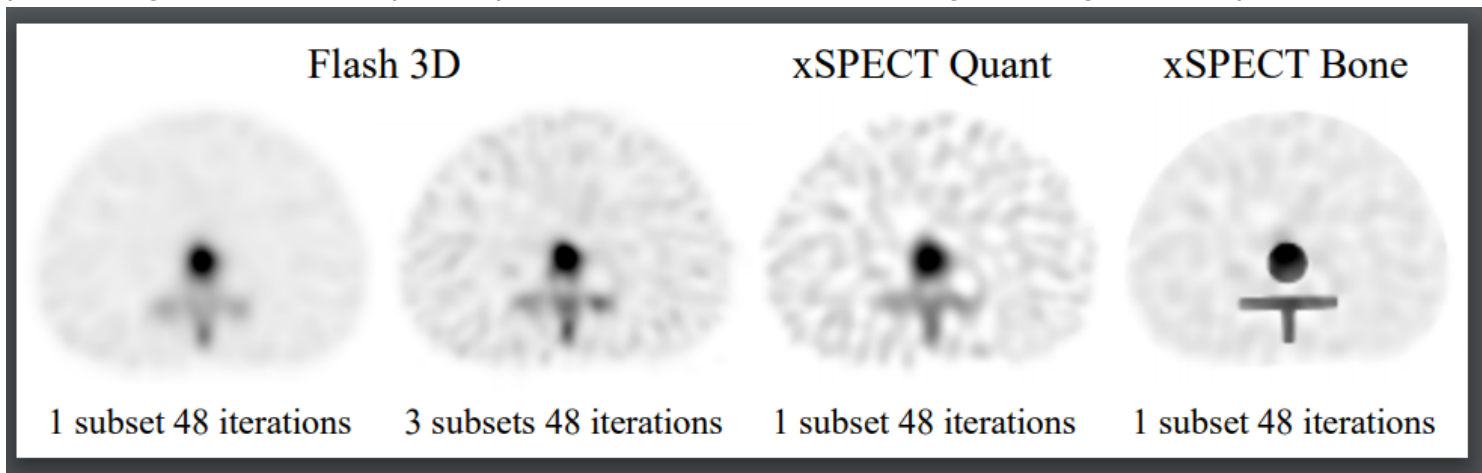


Figure 5

Representative transaxial images of SPECT datasets including three reconstructions at TBR4. Reconstructed images showed the xSPECT and F3D images with 1 subset and with 3 subsets at 48 iterations, respectively.

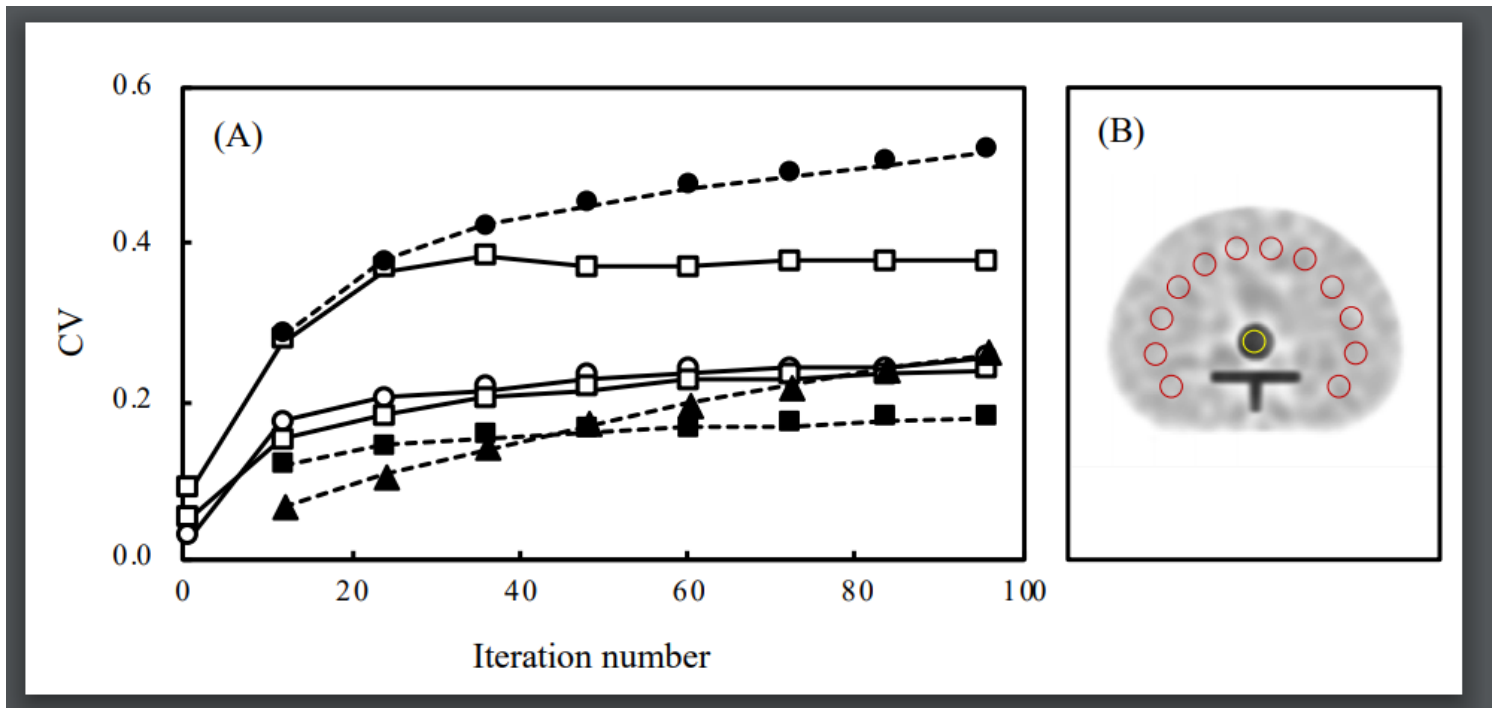


Figure 6

The coefficient of variance (CV) measurement in the ROI placed at the center of the vertebral body. (A), The CV as a function of iteration numbers. The black line is the CV of the vertebral body and the dot line in black is the background CV, respectively. \square , Flash 3D (F3D); \square , xSPECT Quant (xQ); \square , xSPECT Bone (xB). (B), A sample measurement of an xB image at 1 subset and 48 iterations.

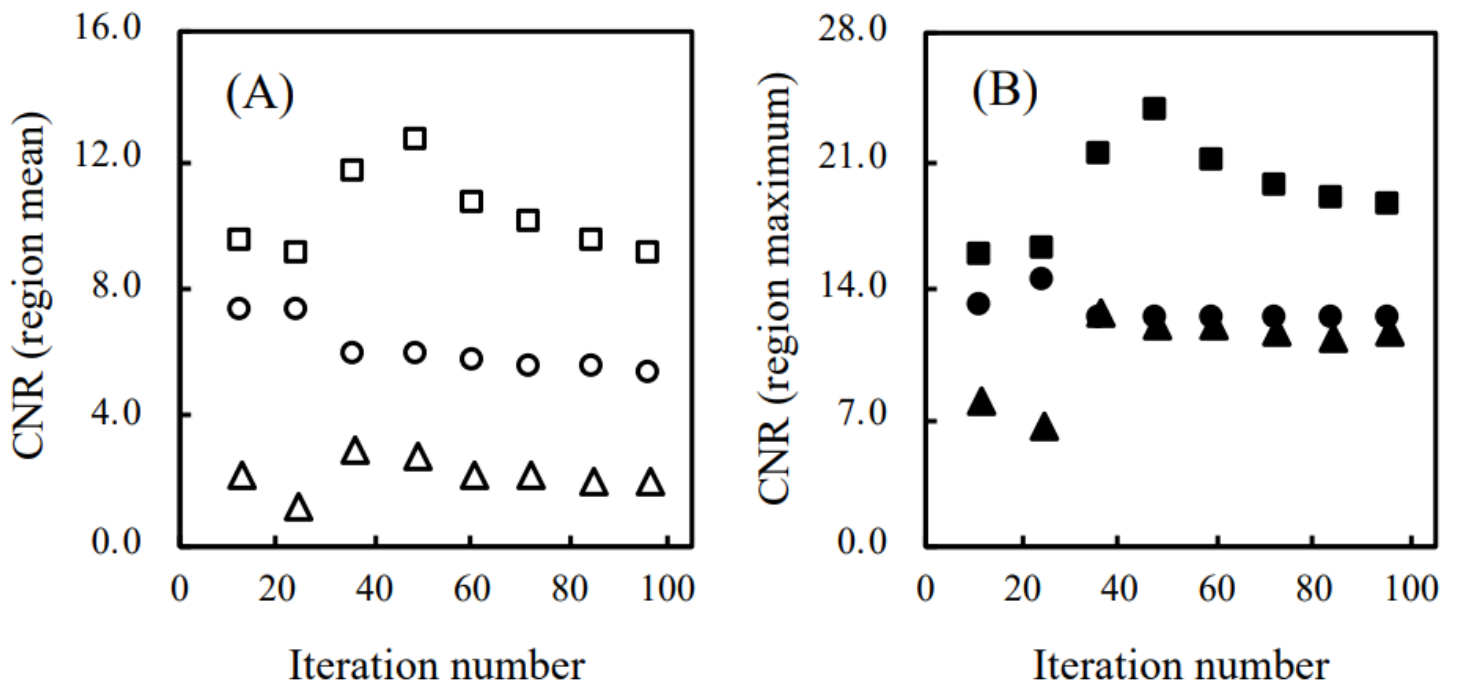


Figure 7

The contrast-to-noise ratio (CNR) measured by activity concentrations for the hot spheres and normal bone at TBR 4. (A), The mean CNR as a function of iteration numbers. (B), The maximum CNR as a function of iteration numbers. \square , Flash 3D (F3D); \circ , xSPECT Quant (xQ); \triangle , xSPECT Bone (xB).

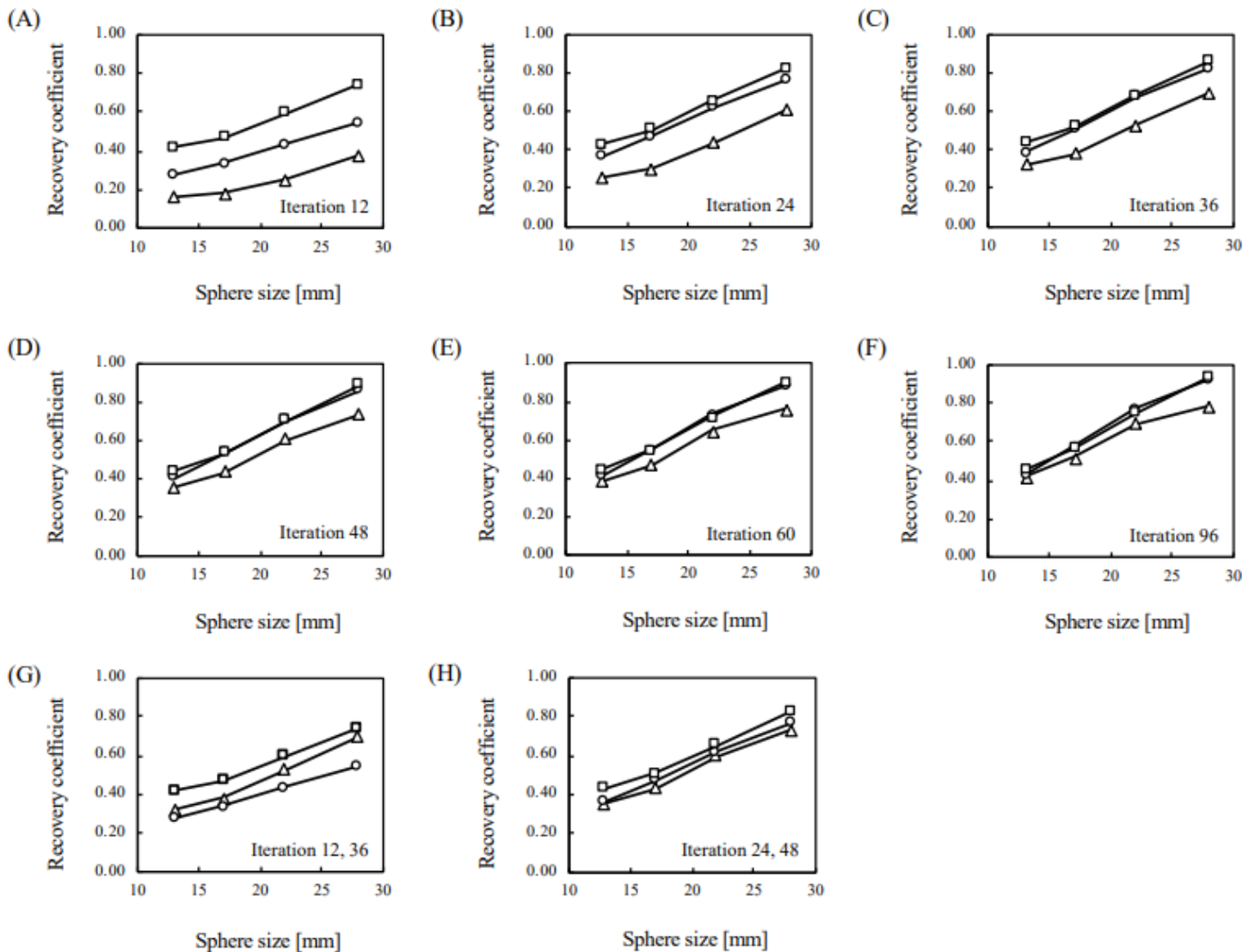


Figure 8

Recovery coefficients of three reconstructions at various numbers of iterations. The numbers of iterations in A, B, C, D, E and F are 12, 24, 36, 48, 60 and 96, respectively. In addition, the numbers of iterations in G and H show the different parameters of 36 and 48 in Flash 3D and 12 and 24 in xSPECT, respectively. \square , Flash 3D; \circ , xSPECT Quant; \triangle , xSPECT Bone.

Supplementary Files

This is a list of supplementary files associated with this preprint. Click to download.

- [Equation.docx](#)